Supporting Information

for

The oxygen-resistant [FeFe]-hydrogenase CbA5H harbors an unknown radical signal

Melanie Heghmanns[1‡], Andreas Rutz[2‡], Yury Kutin[1], Vera Engelbrecht[2], Martin Winkler[3], Thomas Happe[2*], Müge Kasanmascheff[1*]

[1] Technical University of Dortmund, Department of Chemistry and Chemical Biology, Otto-Hahn-Straße 6, 44227 Dortmund, Germany

[2] Ruhr University Bochum, Faculty of Biology and Biotechnology, Photobiotechnology, Universitätsstr. 150, 44801 Bochum, Germany

[3] Technical University of Munich Campus Straubing for Biotechnology and Sustainability, Professorship for Electrobiotechnology, Uferstrasse 53, 94315 Straubing, Germany

[‡] Contributed equally

[*] Corresponding authors (thomas.happe@rub.de, muege.kasanmascheff@tu-dortmund.de)

Material and Methods

Cw EPR spectroscopy

All X-band cw EPR spectra recorded at 100 K were obtained using a Bruker EMX-Nano Benchtop spectrometer equipped with a continuous-flow nitrogen cryostat. The experimental conditions were 100 kHz modulation frequency, 4 G modulation amplitude, and variable parameters given in figure captions.
X-band cw EPR measurements shown in Figures S6 and S12 were performed at 15-20 K using a Bruker ELEXSYS E580 X-band EPR spectrometer, equipped with a Bruker ER 4118X-MD5 resonator and an Oxford Instruments ER 4118CF cryostat. The experimental conditions were 100 kHz modulation frequency, 7 G modulation amplitude, and variable parameters given in figure captions. All EPR spectra were baseline-corrected using MATLAB. If not stated otherwise, all spectra were normalized to the given frequency, protein concentration, microwave power, and the number of scans. Spectral simulations were performed with *EasySpin* using the implemented *pepper* function. [1]

Pulsed EPR spectroscopy

Pulsed EPR (electron spin echo detected EPR, ESE-detected EPR) field-sweep experiments, using a two-pulse Hahn spin-echo sequence $\pi/2–\tau–\pi–\tau–$echo without phase cycling, were carried out on a Bruker ELEXSYS E580 Q-band EPR spectrometer equipped with a Bruker ER 5106QT-2 resonator, an Oxford Instruments CF935 cryostat and Oxford Instruments MercuryiTC temperature controller. The cryogenic temperatures were kept with a sufficiently high flow of liquid He. If not stated otherwise, spectra were acquired in the overcoupled mode with gaussian $\pi/2$- and π-pulses whose lengths were optimized before each experiment and varied between 10–13 and 20–26 ns, respectively. The interpulse delay τ was usually set between 220–300 ns and the shot repetition time (SRT) between 0.3–25 ms, depending on the sample and temperature. As a rule, the SRT was long enough to prevent saturation. For most measurements at 10 K, however, an SRT of 3 ms was chosen for time-efficient measurements: prolonged SRTs led to higher signal intensities, but no change in line shape was observed. The EPR spectra were baseline-corrected using MATLAB. If not stated otherwise, all spectra were normalized to the given frequency, protein concentration, video gain, shots per point, and number of scans. Spectral simulations were performed with *EasySpin* using the implemented *pepper* function. [1]

Electron Nuclear Double Resonance (ENDOR)

ENDOR experiments were carried out at 17 K and 20 K using a Bruker EN 5107D2 resonator and an AR 600 W radiofrequency (RF) amplifier (AR 600A225A). Davies ENDOR spectra were recorded using the following microwave pulse sequence: $\pi–T–\pi/2–\tau–\pi–\tau–$echo. An RF pulse of variable frequency was applied during the time interval T. The RF pulse length was chosen based on the nucleus: either ^{1}H (17 µs) or ^{2}H/^{57}Fe (40 µs). The first π-pulse was a rectangular-shaped inversion pulse of 130 ns. Mims ENDOR experiments were carried out at 17 K using the following stimulated-echo pulse sequence: $\pi/2–\tau–\pi/2–$T$–\pi/2–\tau–$echo with τ = 300 ns.

ATR-FTIR spectroscopy

Attenuated total reflectance Fourier transform spectroscopy was performed on a Bruker Tensor II spectrometer (Bruker Optik, Germany), equipped with a nine reflection ZnSe/Si crystal (Microm ATR Vision, Czitek). All measurements were conducted under anoxic conditions (1.5 % H_2, 98.5 % N_2) at 25 °C. The FTIR spectra were recorded from 4000 – 1000 cm^{-1} with a resolution of 2 cm^{-1}. The protein film was dried with a constant gas stream for around 10 minutes and re-humidified with an aerosol by purging a buffer containing compartment.

Expression and purification

E. coli strain BL21 (DE3) ΔiscR was transformed with the expression plasmid pET21b containing the desired gene for protein expression. The codon-optimized CBA5H gene from *Clostridium beijerinckii* (NCBI GenBank: KX147468.1) and the CPI gene from *Clostridium pasteurianum* (NCBI GenBank: WP_004455619.1) was used to express strep-tagged apo-[FeFe]-hydrogenases (lacking the $[2Fe]_H$ subcluster). [2] Expression and purification was conducted under strictly anaerobic conditions as described previously if not stated otherwise. [3] Affinity chromatography was performed using Strep Tacting High-capacity resin (IBA GmBH). The protein concentration was determined by Bradford assay, and purity was verified by SDS-PAGE (polyacrylamide gel electrophoresis), as shown in the Figure below. [4,5] The metal content of apo-CbA5H protein was quantified by ICP-AES (inductively coupled plasma atomic emission spectroscopy) measurements to 12 ± 1 Fe-atoms per monomer in agreement with the literature. [6] Proteins were stored at −80 °C in 100 mM Tris-HCl buffer pH 8 with 2 mM sodium dithionite (NaDT), if not stated otherwise. For NaDT-free protein preparations (termed NaDT-free in the following), sodium dithionite was removed via size exclusion chromatography (NAP 5 column, GE healthcare). The protein solution was stored in 100 mM Tris-HCl buffer pH 8. Details of all the samples used in this work are given in Table S1.

Expression of ^{57}Fe labeled apoprotein

Protein expression was performed in M9 minimal media (without iron source) supplemented with ^{57}Fe (Euroisotope) dissolved in HCl. Approximately 15 mg ^{57}Fe per liter culture was used for the overexpression of the labeled apoprotein. The *E. coli* BL21 (DE3) ΔiscR cells were grown until an OD of 0.6 and then transferred into an anaerobic glovebox. All other steps of expression and purification were conducted as previously described. [3] The ^{57}Fe-labeled apoprotein was reconstituted with the $[2Fe]_H$ mimic synthesized with ^{56}Fe (see below).

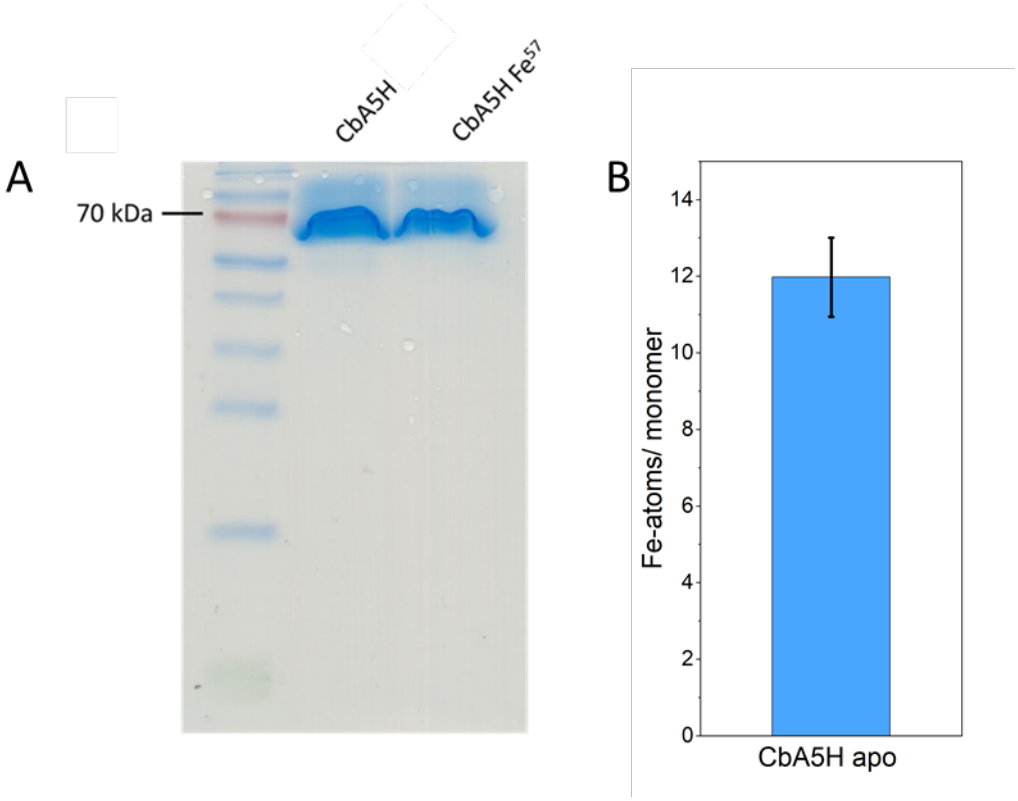

SDS-PAGE and Fe-quantification. (**A**) Lane 1: Protein Marker, Lane 2: CbA5H expressed under standard conditions, Lane 3: ^{57}Fe-labeled CbA5H. The molecular weight of the CbA5H monomer is 75 kDa. (**B**) Fe-atoms quantified by ICP-AES measurements for apo-CbA5H.

***In vitro* maturation**

Apoproteins were incubated on ice for 1 hour with a 10-fold molar excess of the artificially synthesized $[2Fe]_H$ cofactor mimics $[2Fe(SCH_2XCH_2S)(CO)_4(CN)_2]^{2-}$ (X = NH (adt), X = CH_2 (pdt)) to reconstitute active protein as described earlier. [7,8] Holoproteins and excess $[2Fe]_H$ were separated by size exclusion chromatography (NAP 5 column, GE healthcare).

CbA5H sample preparation

For H_2-treated samples, anaerobically isolated CbA5H protein solution was exposed for 45 minutes in a sealed suba tube to a humidified gas stream of 100 % H_2. All O_2-treated samples were initially treated with H_2 and subsequently exposed to a humidified O_2 (100 %) gas stream.

H_2-O_2 cycle of as-isolated CbA5H

For the H_2-O_2 cycle, an anaerobically isolated protein solution of CbA5H (400 µM) was first treated with H_2 (45 min) and then gassed with O_2 (20 min) in two repetitive cycles under the same conditions. Samples were taken after the respective treatment. The ESE-detected Q-band EPR spectra shown in Figure 3 in the main text were recorded in the critically coupled mode with rectangular pulses. The integrated absorption spectra were used as an approximation for the overall signal intensities of paramagnetic species in CbA5H. The intensity of the CbA5H^{H2} signal (trace 1, top) decreased by ~40 % after one cycle with O_2 and H_2 (trace 3) that is in accordance with activity data (see Figure S7). The signal intensity of CbA5H^{O2} (trace 2) decreased by ~5 % after treatment with H_2 and O_2 (trace 4). Note that the signal intensities are only valid for the temperature of 10 K and SRT of 3 ms. The features marked with an asterisk are assumed to arise from O_2-damaged FeS clusters, H_{ox}-CO, and/or background impurities. They are only detectable in the critically coupled mode and at lower temperatures

(compare with Figures S2 and S4). To isolate the $g \approx 2.01$ signal (termed $R^{\bullet ox}$) and determine absolute and relative spin concentrations, the same samples were investigated at 100 K via X-band cw EPR (see Figure S4).

Table S1: Information on sample preparations of CbA5H, apo-CbA5H, and CpI with their respective abbreviations (marked in bold), protein concentrations, appearances in figures (M: main text, S: supplemental information), and presence of $R^{\bullet ox}$.

Sample	Concentration /µM	Figure(s)	$R^{\bullet ox}$ present
apo-CbA5H^{NaDT} apo-CbA5H + 10mM NaDT, 10 % glycerol	350	M2, S2	-
apo-CbA5H^{H2} apo-CbA5H +H_2	730	S6, S12	-
apo-CbA5H^{O2} apo-CbA5H + H_2, + O_2	730	M4, S6, S8, S12	-
CbA5H^{NaDT} CbA5H + 10 mM NaDT, 5 % glycerol	530	M2, S1-2	✓
CbA5H^{air} CbA5H + 10mM NaDT, + O_2, 5 % glycerol	530	S8	✓
CbA5H + 100 mM NaDT, 5 % glycerol	500	S1	✓
H_2-O_2-cycle CbA5H + H_2, + O_2, + H_2, + O_2	400	M3, S3-4	✓
aerobically isolated CbA5H^{H2} CbA5H + H_2	970	S6, S11-12	✓
aerobically isolated CbA5H^{O2} CbA5H + H_2, + O_2	970	S6, S11-12	✓
NaDT-free CbA5H^{H2} CbA5H + H_2	490	S1-2, S5, S8-11, S13, S15	✓
NaDT-free CbA5H^{O2} CbA5H + H_2, + O_2	490	M3-4, S5 S8-11, S13, S15, S17, S19-20	✓
CbA5H$_{D2O}$ CbA5H in deuterated buffer + H_2, + O_2	500	S19-20	✓
CbA5H^{HAR} CbA5H + 1mM HAR	430	S5-9	✓
CbA5H^{HAR} + H_2 CbA5H + 1mM HAR, + H_2	430	S9	✓
^{57}Fe-CbA5H^{O2} ^{57}Fe-labeled apo-CbA5H maturated with $[2^{56}Fe]_H$	400	M5, S17-18, S20	✓
CbA5H-C367D^{O2} CbA5H variant with Cys to Asp exchange at position 367	700	M4, S15	✓
CbA5H(pdt)^{H2} CbA5H maturated with pdt, + H_2	500	S13	-
CbA5H(pdt)^{O2} CbA5H maturated with pdt, + H_2, + O_2	500	M4, S13	-
CpI^{H2} CpI + H_2	270	S10	-
CpI^{O2} CpI + H_2, + O_2	270	M4, S10	-

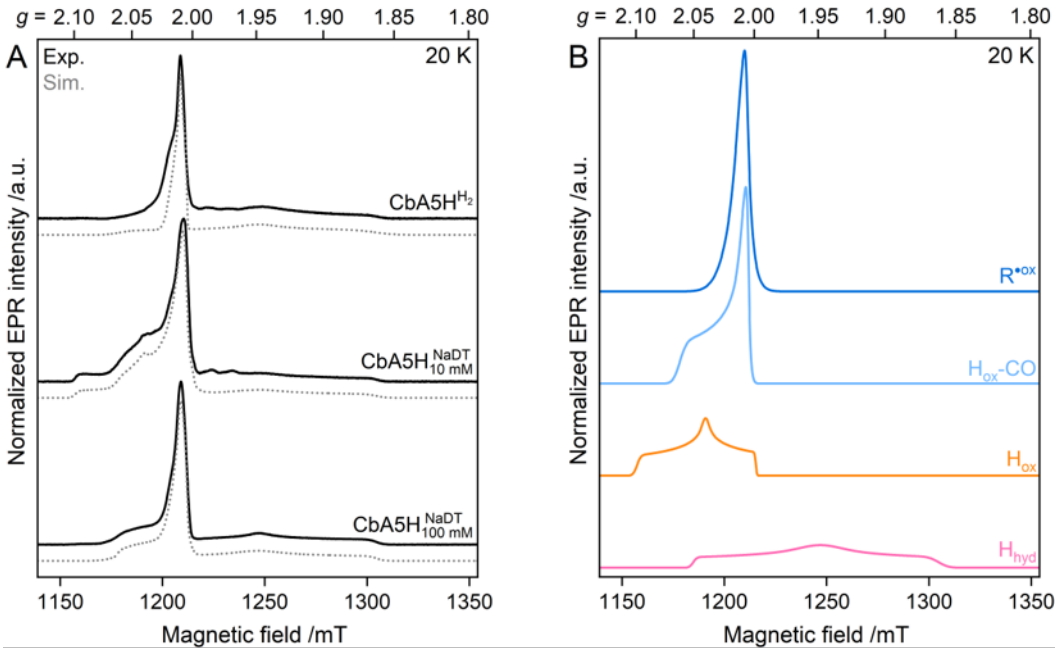

C

Species	Relative weights in %		
	CbA5H^{H2}	CbA5H^{NaDT} (10 mM)	CbA5H^{NaDT} (100 mM)
R$^{\bullet ox}$	51	27	33
H_{ox}-CO	-	31	30
H_{ox}	-	20	-
H_{hyd}	49	22	37

Figure S1. Pulsed EPR spectra (34 GHz, T = 20K) of CbA5H treated with H_2 (NaDT-free) and 10 or 100 mMNaDT. (**A**) Experimental spectra (black traces) and simulations (grey dotted traces) with varying contributions from (**B**) the $g \approx 2.01$ signal (termed R$^{\bullet ox}$, blue), H_{ox}-CO (light blue), H_{ox} (orange), and H_{hyd} (pink). (**C**) Relative weights of the paramagnetic species used in the simulations for the three samples (for g-values, see Table S2). The values are only valid for T = 20 K and an SRT of 0.5 ms. The short SRT was used to suppress R$^{\bullet ox}$ and improve spectral simulations for the remaining species. The full simulations were obtained by simulating four species simultaneously, with their relative weights having an uncertainty of ± 5 %. While the spectrum of CbA5H^{H2} shows contributions from R$^{\bullet ox}$ and H_{hyd}, the 10 mM NaDT-reduced spectrum has additional features of H_{ox} and H_{ox}-CO. Under stronger reducing conditions (100 mM NaDT), H_{hyd} predominates, while the contribution of H_{ox} is negligible. This observation is in accordance with H_{hyd} being only observable at low potentials (< 400 mV) and H_{ox} dominating the hydrogenase EPR spectra at higher potentials. [9] We could isolate R$^{\bullet ox}$ at temperatures above 70 K (see also Figures S2 and S4).

Table S2. Simulation parameters of paramagnetic species observed in CbA5H with $g_1 > g_2 > g_3$. The *g*-values of CbA5H (error given in brackets) were obtained from several different sample preparations recorded at different temperatures and frequencies, where certain species dominated the spectrum (see also Figure S2). Note that *g*-strain was the only line broadening mechanism employed in the simulations. The $R^{\bullet ox\ *}$ species arising in C367D[O2] reveals slightly different simulation parameters.

Species	*g*-tensor			*g*-strain		
$R^{\bullet ox}$	2.019(4)	2.010(3)	2.006(3)	0.030	0.010	0.002
$R^{\bullet ox\ *}$	2.015(3)	2.012(3)	2.007(2)	0.012	0.001	0.004
FS4 (axial)	2.09(1)	1.92(1)	1.92(1)	0.03	0.03	0.06
FS4 (rhombic)	2.03(1)	1.94(1)	1.84(1)	0.03	0.01	0.05
H_{ox}	2.099(1)	2.039(1)	1.999(1)	0.007	0.005	0.002
H_{ox}-CO	2.060(4)	2.008(1)	2.006(2)	0.011	0.008	0.002
H_{hyd}	2.050(20)	1.948(1)	1.862(1)	0.006	0.029	0.013

Table S3. *g*-values of paramagnetic H-cluster states observed in CbA5H with $g_1 > g_2 > g_3$ in comparison to literature values. The asterisks mark the species in which *g*-tensors arise from the H_{hyd} state.

Protein	H_{hyd} or H_{trans}			H_{ox}			H_{ox}-CO			Ref.
*Cb*A5H*	2.050(20)	1.948(1)	1.862(1)	2.099(1)	2.039(1)	1.999(1)	2.060(4)	2.008(1)	2.006(2)	this work
*Cr*HydA1*	2.07	1.93	1.88	2.100	2.037	1.996	2.052	2.007	2.007	[10–12]
*Dd*H	2.06	1.96	1.89	2.10	2.04	2.00	2.06	2.00	2.00	[13]
*Dd*V	2.07	1.96	1.89	2.11	2.05	2.00	2.06	2.00	2.00	[14–16]
*Cp*I				2.097	2.0392	1.999	2.0725	2.006	2.006	[17]
*Me*HydA				2.093	2.041	1.999	2.061	2.007	2.007	[18]

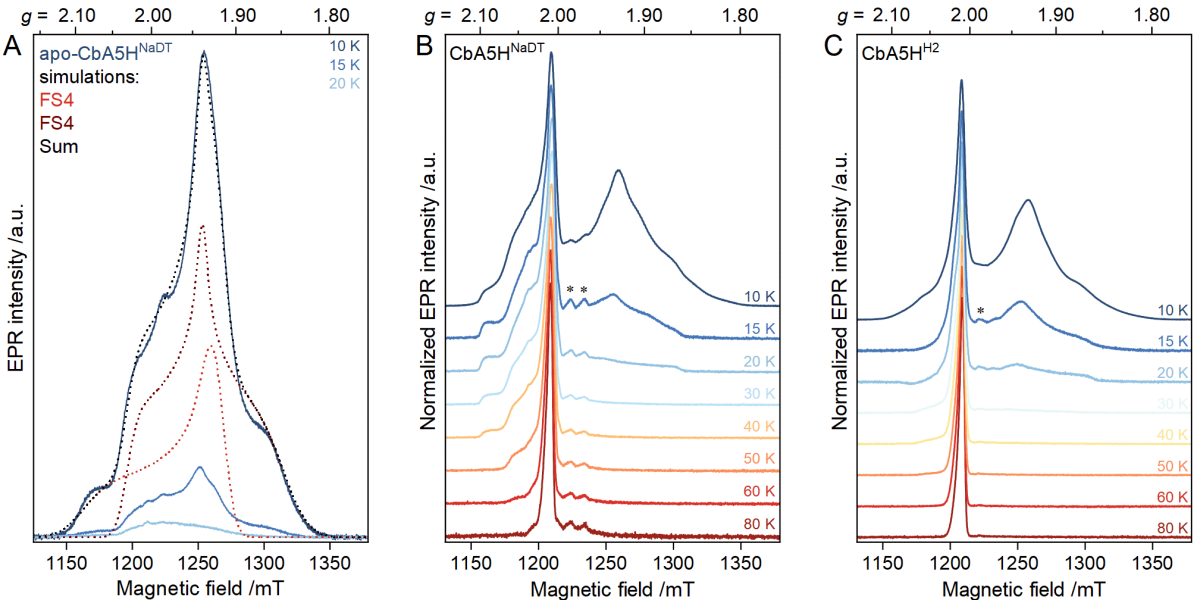

Figure S2. Temperature-dependent pulsed EPR spectra (34 GHz) of reduced apo- and holo-CbA5H. (**A**) reduced (10 mM NaDT) apo-CbA5H, (**B**) reduced (10 mM NaDT) CbA5H and (**C**) H_2-treated, NaDT-free CbA5H. The apo-CbA5H^{NaDT} spectrum at 10 K in A (dark blue) was simulated as a sum (dotted black line) of two contributions from [4Fe4S] clusters (FS4, dotted lines) with rhombic (62 % weight, dark red) and axial (38 % weight, light red) line shape. The simulation parameters are displayed in Table S2. Although there probably exist three [4Fe4S] clusters in the apo-CbA5H, our attempts to simulate the spectrum with three species failed. This might be due to the incomplete reduction of $[4Fe4S]_H$. Note that redox potentiometry or cluster knockouts are necessary to confirm and assign the spectral simulations to their respective cluster. The spectra in B and C were normalized to their maximum signal intensities, and Mn^{2+} impurity signals are marked with asterisks. The EPR spectrum of apo-CbA5H is broadened beyond detection above 20 K, indicating (i) the absence of H-cluster states, (ii) the presence of fast-relaxing $[4Fe4S]^{1+}$ clusters, [19,20], and (iii) lack of accessory $[2Fe2S]^{1+}$ clusters found, e.g., in CpI. [21] In B and C, the rhombic H_{hyd} state is observable up to 25 K, the rhombic signal from H_{ox} is observed below 50 K, and the axial signal of H_{ox}-CO is observed below 60 K. The $g \approx 2.01$ signal (termed $R^{\bullet ox}$) was the only detectable species above 70 K (see Figure S4 and Table S2 for more details).

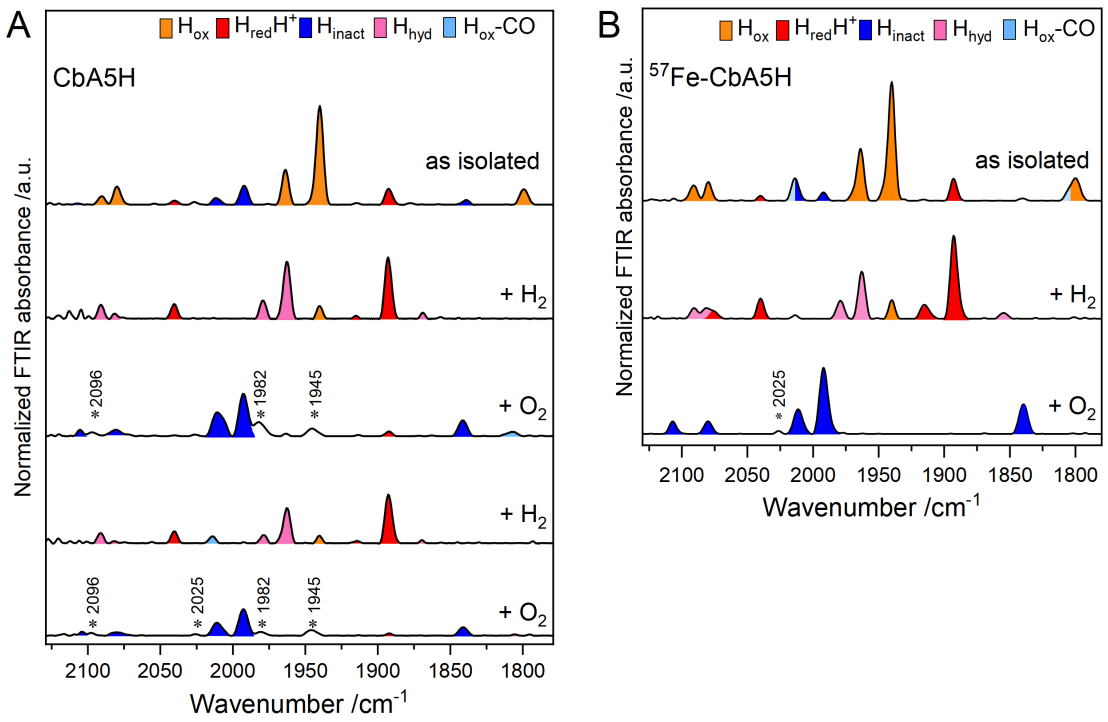

Figure S3. IR-vibrational spectra of CbA5H monitored *via* ATR-FTIR-spectroscopy. (**A**) As-isolated CbA5H protein solution (400 µM, 0.1 M Tris-HCl, pH 8) was purged alternately with H_2 and O_2. The vibrational frequencies are associated with different redox states and are colored accordingly. The contributions of $H_{red}H^+$ and H_{hyd} decreased by approximately 39 % and 47 % during the second H_2 treatment, respectively. The signal intensity of H_{inact} decreased by about 40 % in the second O_2 cycle, indicating that H_{inact} is not directly associated with the $g \approx 2.01$ species (termed $R^{\bullet ox}$), as the latter only decreases by approximately 5–10 % throughout the cycle (see Figure 3 in main text and S4). Asterisks represent unassignable bands, which are suggested to arise from oxygenation of bridging thiolates and were observed to induce a shift of 6–19 cm^{-1}. [22] Swanson *et al.* reported similar shifts for HydA1 after prolonged exposure to O_2. [23] (**B**) IR-vibrational spectra of ^{57}Fe-CbA5H samples utilized for EPR measurements. As-isolated samples were purged with H_2 and subsequently with O_2. Aliquots were taken for EPR and FTIR measurements to verify redox state populations. Approximately 50 % of the cluster intensities remain after O_2 purging compared to the H_2-treated sample. H_2-reduced cluster intensities of ^{57}Fe-CbA5H decrease by about 28 % after treatment with O_2.

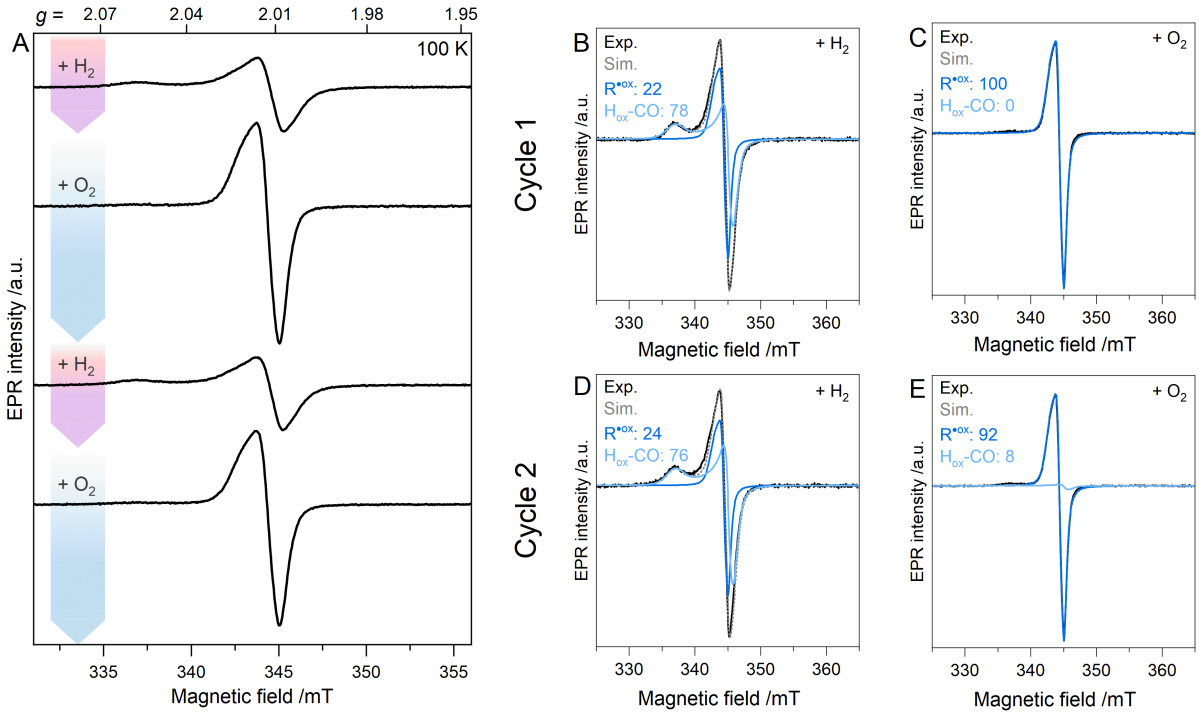

Sample	Spin concentration /spins mol^{-1}	Relative weight /%	
		R•ox	Hox-CO
H_2 (1)	0.077	22	78
O_2 (1)	0.084	100	0
H_2 (2)	0.078	23	76
O_2 (2)	0.079	92	8

Figure S4. Spectral analysis and simulation of cw EPR spectra (9.7 GHz, T = 100 K) within the H_2-O_2 cycle. (**A**) H_2-O_2 cycle of as-isolated CbA5H (see Figure 3 in the main text for pulsed EPR spectra at T = 10 K). (**B–E**) The experimental spectra were simulated with varying contributions of two species, R•ox (blue) and Hox-CO (light blue), with the respective weights (in %) given in the table (see Table S2 for respective *g*-values). The spin concentrations were quantitated by double integration of the cw EPR spectra recorded under non-saturating conditions at X-band and 100 K. The standards for spin quantification were 1 mM CuEDTA and tyrosyl radical, Y_{122}•, residing in *E. coli* class Ia ribonucleotide reductase with a known concentration. We determined R•ox concentrations of at least three distinct CbA5H^{O2} samples from different sample preparations. The highest and lowest amounts were 0.15 and 0.085 spins/mol, respectively, and are in the expected error range of 30 %. [24] The signal intensity of R•ox observed in the shown H_2-O_2 cycle grows by a factor of five upon treatment with O_2 and loses approximately 13 % intensity throughout the cycle. Note that the detected spin concentrations are only valid for the given experimental temperatures. The relative contributions of R•ox and Hox-CO to CbA5H^{H2} at 100 K are 22 % and 78 %, while these values change to 51 % and below 5 %, respectively, when the experiment is conducted at 20 K (Figure 3 and S1). Similar spin concentrations of H-cluster states and variation in optimal temperatures for their EPR detection are observed in other hydrogenases. [13,25] Experimental conditions: 3–10 mW power; 1.28 ms time constant; 80 ms conversion time; 100 s sweep time, 4–5 scans.

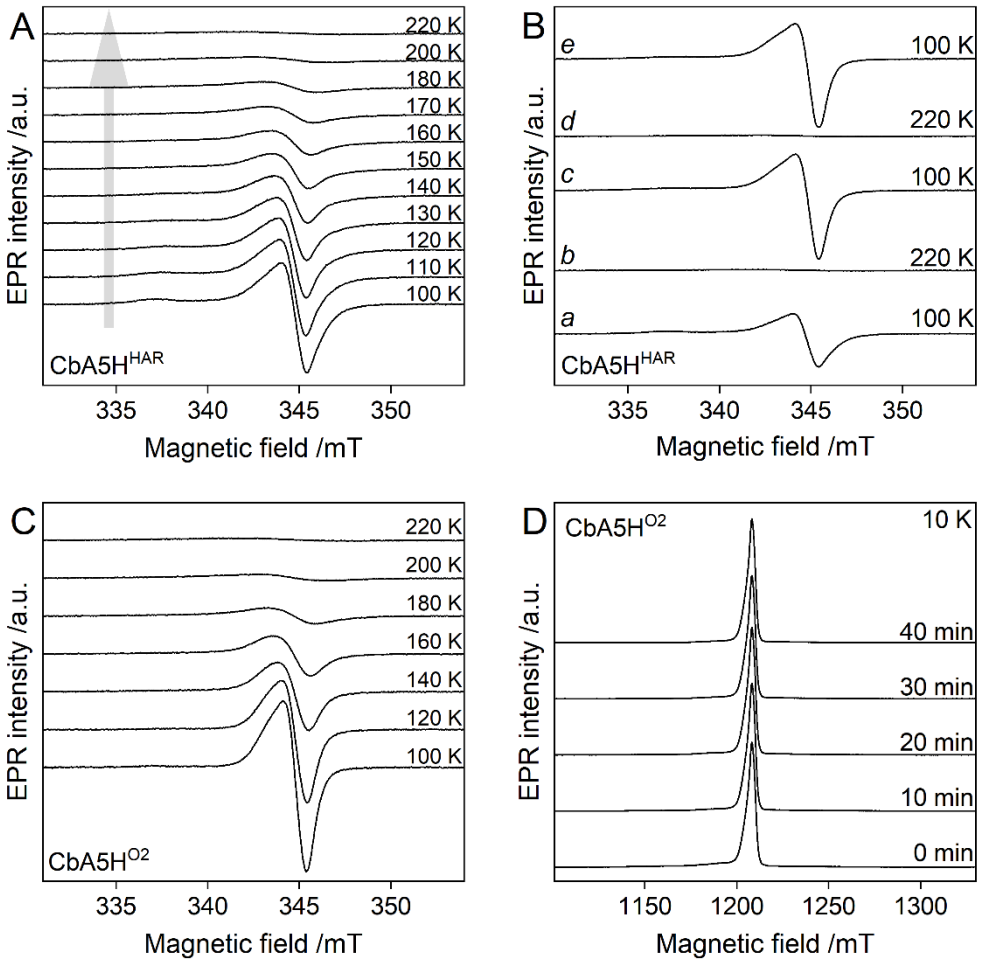

Figure S5. Temperature-dependent EPR spectra of two differently oxidized CbA5H samples with cryo-annealing at T = 220 K and in dry ice. (**A**) Temperature-dependent cw EPR spectra (9.7 GHz, T = 100–220 K) of CbA5H treated with 1 mM HAR were plotted with constant spacing. (As shown in Figure S9, HAR has a similar effect on CbA5H as O_2.) (**B**) Spectra of the same sample were recorded alternately at 100 K and 220 K. Spectra *a* and *b* are the first and last traces shown in A. Spectrum *c* showed a 32 % increase in intensity, possibly due to remaining, previously unreacted HAR from the sample preparation. Spectrum *d* was obtained after 10 min at 220 K. The spectrum *e*, recorded subsequently, showed no signal intensity or line shape change. Experimental conditions: 10 mW power, 1.28 ms time constant, 81 ms conversion time, 77 s sweep time, 5–11 scans. (**C**) Temperature-dependent cw EPR spectra (9.7 GHz, T = 100–220 K) of O_2-oxidized, NaDT-free CbA5H. Experimental conditions: 3 mW power; 1.28 ms time constant; 50 ms conversion time; 50 s sweep time, 3–12 scans. (**D**) Pulsed EPR spectra (34 GHz, T = 10 K) were recorded in a critically coupled cavity with rectangular pulses after 0, 10, 20, 30, and 40 min storage on dry ice (~195 K). The top trace corresponds to a cumulative storage time of 100 min. The measurements shown in panel D were conducted before the ones in C using the same sample. The signal amplitude and shape remained unchanged.

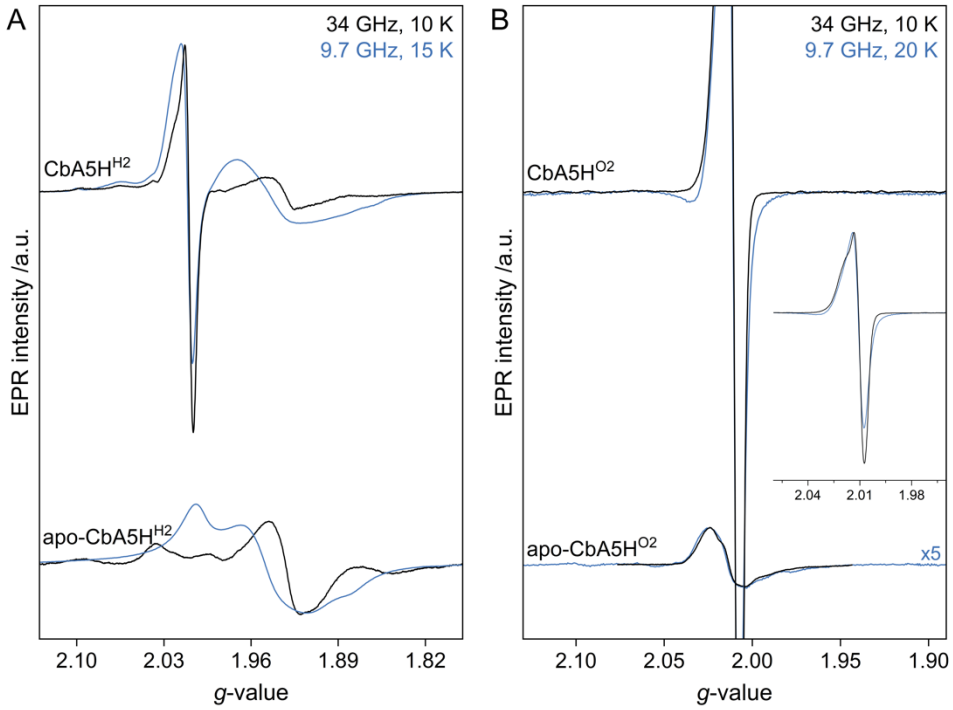

Figure S6. Comparison of cw EPR spectra (9.7 GHz, T = 15–20 K, blue) and pulsed EPR spectra (34 GHz, T = 10 K, black) of anaerobically isolated apo-CbA5H and aerobically isolated holo-CbA5H treated with H_2 or O_2. (**A**) Spectra of $CbA5H^{H2}$ and apo-$CbA5H^{H2}$ and (**B**) spectra of $CbA5H^{O2}$ and apo-$CbA5H^{O2}$ (multiplied by five) with the inset showing the full spectrum of $CbA5H^{O2}$. All spectra were plotted with a common *g*-scale. The intensities of the pulsed EPR spectra were adjusted to the cw EPR spectra for better comparison. The distinct spectral patterns of apo-$CbA5H^{H2}$ observed at X- and Q-band are a strong indicator of spin-spin interaction between FS4A, FS4B, and $[4Fe4S]_H$. [26,27] This observation is not surprising as these clusters are adjacent to each other (≤ 15 Å apart). [28] In contrast, the spectral line shapes of $CbA5H^{O2}$ and apo-$CbA5H^{O2}$ do not change with the frequency. The cw EPR intensity of $CbA5H^{O2}$, originating from $R^{\bullet ox}$, is one order of magnitude higher than that of apo-$CbA5H^{O2}$, which only exhibits residual $[3Fe4S]^+$ clusters due to oxidation damage to [4Fe4S] clusters. [29] Experimental conditions for (i) H_2-reduced samples: 20 K; 1.5 µW power; 100 ms conversion time and 205 s sweep time and (ii) for O_2-oxidized samples: 10 K; 0.47 mW power; 80 ms conversion time and 40 s sweep time.

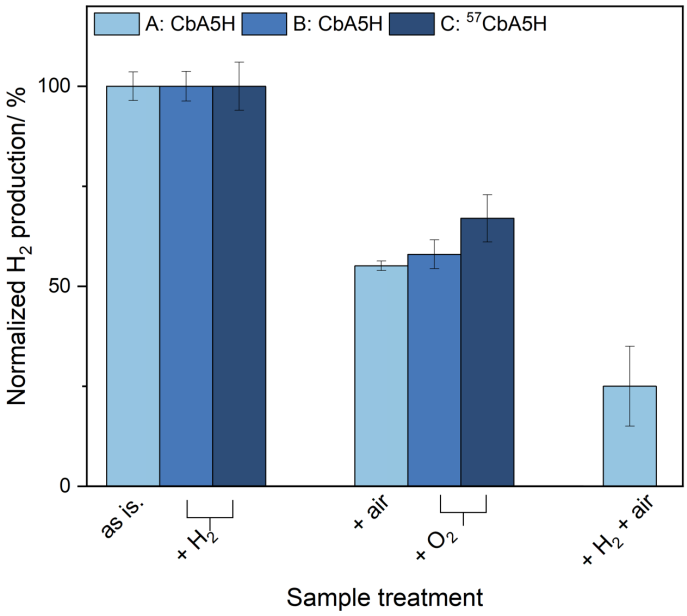

Figure S7: H_2-production activities of CbA5H (wild type and ^{57}Fe-labeled) prior and after exposures to H_2, air and O_2. Hydrogen production activities were determined with a standard assay, as reported earlier. [8] (**A**) H_2-production activities of wild-type CbA5H prior and after air and H_2 exposures. The enzyme stock solution was prepared without NaDT to ensure the absence of oxygen-scavenging reagents. Before further treatment, one aliquot was taken from the stock solution, termed "as isolated" (as is.). Next, the enzyme solution was incubated for 20 min in the air. Aliquots were taken and termed "air". The remaining protein solution was reactivated with 100 % H_2 (45 min) and incubated for an additional 20 min in the air to prepare the aliquot termed "H_2 + air". To determine the hydrogen production activity of previously prepared aliquots, 400 ng enzyme was mixed with 0.1 M potassium phosphate buffer (pH 6.8), 100 mM NaDT and 10 mM methyl viologen. The assay solution was incubated in a sealed suba vessel for 20 min at 37° C under constant shaking. The H_2 production rate was determined via GC-FID (gas chromatography-flame ionization detector). Error bars represent the standard deviations from three technical replicates. (**B, C**) H_2-production activities of wild type and ^{57}Fe-labeled CbA5H before and after exposure to H_2 and O_2. The protein solution was treated with 100 % H_2 (60 min) and incubated for an additional 20 min with 100 % O_2. 400 ng enzyme was mixed with 0.1 M potassium phosphate buffer (pH 6.8), 100 mM NaDT and 10 mM methyl viologen. The assay solution was incubated in a sealed suba vessel for 20 min at 37°C under constant shaking. The H_2 production rate was determined via GC-FID. Activities for H_2-treated CbA5H: 2907 ± 107 µmol H_2 × min^{-1} × mg protein^{-1} and for ^{57}Fe-CbA5H: 2734 ± 163 µmol H_2 × min^{-1} × mg protein^{-1}. After O_2 treatment, the activity decreased by 42 % for CbA5H (1690 ± 60 µmol H_2 × min^{-1} × mg protein^{-1}) and by 33 % for ^{57}Fe-CbA5H (1825 ± 108 µmol H_2 × min^{-1} × mg protein^{-1}).

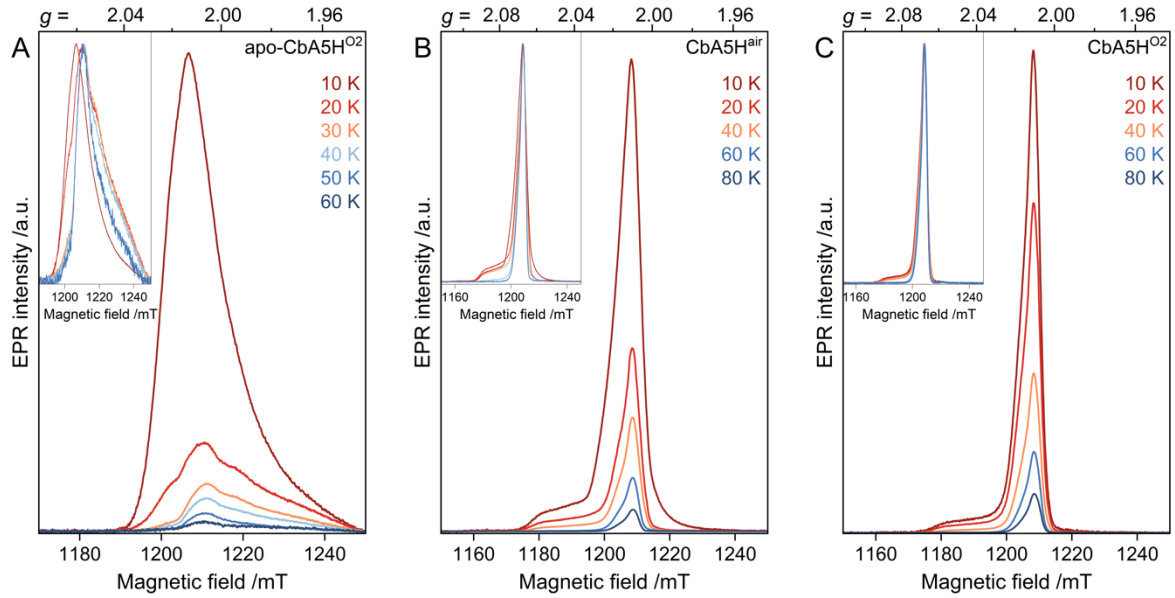

Figure S8. Temperature-dependent pulsed EPR spectra (34 GHz) of oxidized holo- and apo-CbA5H and comparison of air and O_2 for oxidation. (**A**) Spectra of apo-CbA5H^{O2} (SRT: 3.0 – 0.3 ms); (**B**) spectra of air-oxidized holo-CbA5H^{air} (SRT: 25.0 – 0.5 ms); (**C**) spectra of O_2-treated, NaDT-free, holo-CbA5H^{O2} (SRT: 25.0 – 0.5 ms). Note that the third sample had undergone cryo-annealing (see Figure S5 C–D) and thawing. Therefore, it exhibits a contribution from H_{ox}-CO that arises from degraded FeS clusters. This is usually not observed in O_2-oxidized samples (compare Figures S4, S6, and S11). The insets show the spectra normalized to their maximum signal intensity (apo-CbA5H^{O2} measured at 60 K was left out for better visualization due to its low S/N ratio). The spectra of apo-CbA5H^{O2} (A) are observable up to 60 K showing characteristics of an oxidized [3Fe4S]$^{+}$ cluster ($g_{max} \approx 2.03$). [30] In addition to R$^{\bullet ox}$, two more species were detected in holo-CbA5H^{air} (B). First, a minor contribution of the [3Fe4S]$^{+}$ cluster signal was present at 10 K. Second, using air for oxidation led to the formation of H_{ox}-CO, which is observable up to 50 K. At temperatures ≥ 60 K, R$^{\bullet ox}$ is the only observable EPR signal.

Corrigan et al. [6] observed an EPR signal similar to R$^{\bullet ox}$ in an as-isolated CbA5H sample upon oxidation. They ascribed it to a [3Fe4S]$^{+}$ cluster arising from degraded FeS clusters based on free Fe^{3+} present in the oxidized sample. When compared, the spectral features of R$^{\bullet ox}$ are indeed reminiscent of signals typical for oxidized [3Fe4S]$^{1+}$ clusters, including the one observed in apo-CbA5H^{O2}. However, numerous significant properties distinguish it from typical [3Fe4S]$^{1+}$ clusters. First, R$^{\bullet ox}$ is detectable above 100 K (see C). Second, its line shape and temperature dependence are entirely different from those of the [3Fe4S]$^{1+}$ clusters shown in (A) and reported in the literature. [19,30–33] Third, the contribution of R$^{\bullet ox}$ in CbA5H^{O2} is an order of magnitude higher compared to the [3Fe4S]$^{1+}$ cluster observed in apo-CbA5H^{O2} (see also Figure S6). Last, similar amounts of a g = 4.30 signal related to the oxidative degradation of FeS clusters are found in CbA5H^{O2} and apo-CbA5H^{O2} (see Figure S12).

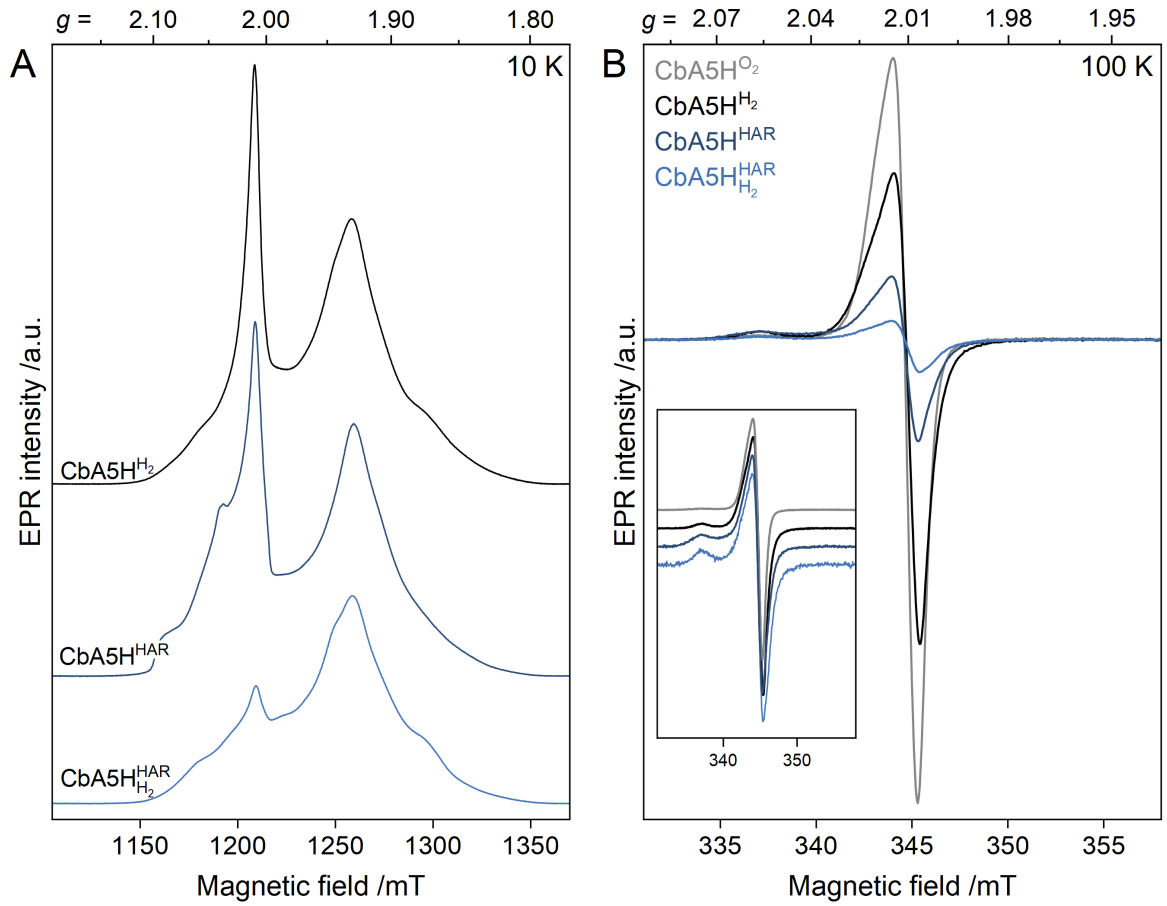

Figure S9. Comparison of EPR spectra of NaDT-free H_2- and O_2-treated CbA5H (CbA5H$^{O2/H2}$) with spectra of CbA5H treated with 1 mM HAR (CbA5H^{HAR}), which was subsequently gassed with H_2 (CbA5H$^{HAR}{}_{H2}$). (**A**) Pulsed EPR spectra (34 GHz, T = 10 K). Using the mild oxidant HAR, a dominant formation of Hox is observed compared to CbA5H^{H2}. Treating CbA5H^{HAR} with H_2 reduces the signal intensity of R$^{\bullet ox}$. (**B**) Cw EPR spectra recorded at 9.7 GHz and T = 100 K. Spectra normalized to their maximum signal intensity are shown with constant spacings in the inset for better comparison. Suppression of fast-relaxing species at 100 K reveals R$^{\bullet ox}$ in all samples, while CbA5H^{H2} and both HAR-treated samples reveal minor contributions from the H_{ox}-CO state (see $g \approx 2.06$). The signal intensity of R$^{\bullet ox}$ obtained from spectral simulations is approximately 80 % lower in the HAR-treated sample than CbA5H^{O2}. This might arise from different sample preparations, considering the differences between HAR and O_2 regarding the molar ratio, accessibility, and reactivity with the protein. X-band experimental conditions: 10 mW power; 1.28 ms time constant; 81 ms conversion time; 61 s sweep time, 3–9scans.

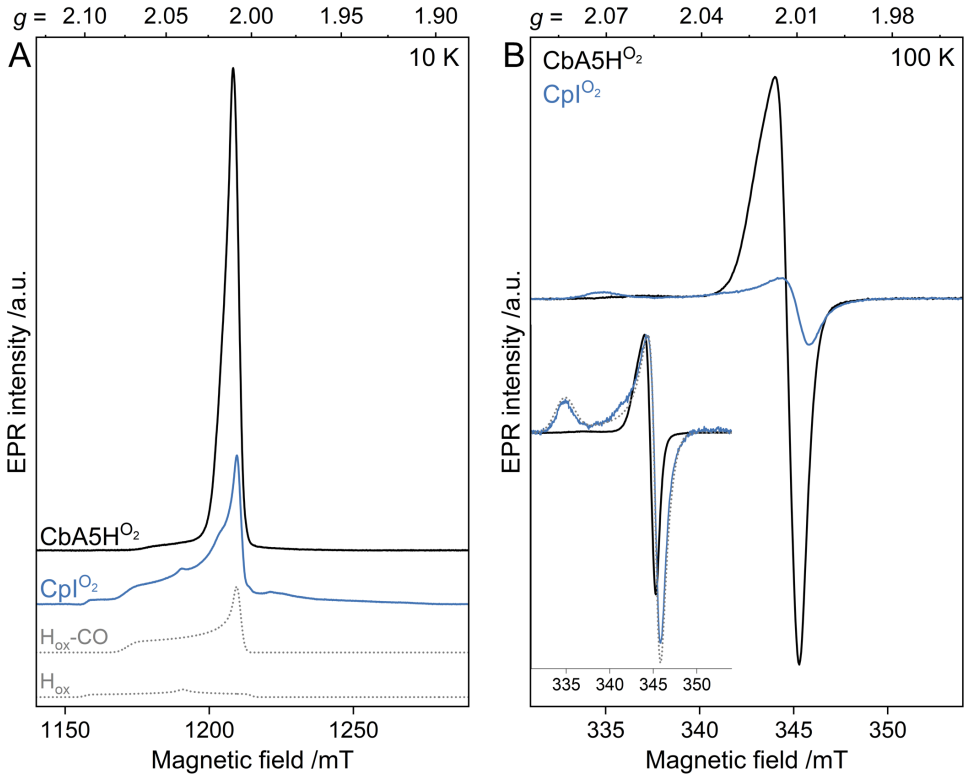

Figure S10. Comparison of EPR spectra of NaDT-free, O_2-oxidized CbA5H^{O2} (black), and CpI^{O2} (blue). The spectra were measured (**A**) via pulsed EPR (34 GHz, T = 10 K) and (**B**) via cw EPR (9.7 GHz, T = 100 K). The latter spectra normalized to their maximum signal intensity are shown in the inset. In contrast to CbA5H^{O2} showing R$^{\bullet ox}$ at both temperatures, the spectrum of CpI^{O2} at 10 K shows contributions from H$_{ox}$ (g =2.10, 2.04, 2.00) and H$_{ox}$-CO (g =2.074, 2.008, 2.006) (simulations shown with grey dotted traces). At 100 K, only a weak signal of H$_{ox}$-CO is observable in CpI (see the grey dotted trace in the inset). X-band experimental conditions for CpI: 3 mW power; 1.28 ms time constant; 80 ms conversion time; 100 s sweep time, 15 scans; for CbA5H^{O2}, see Figure S9.

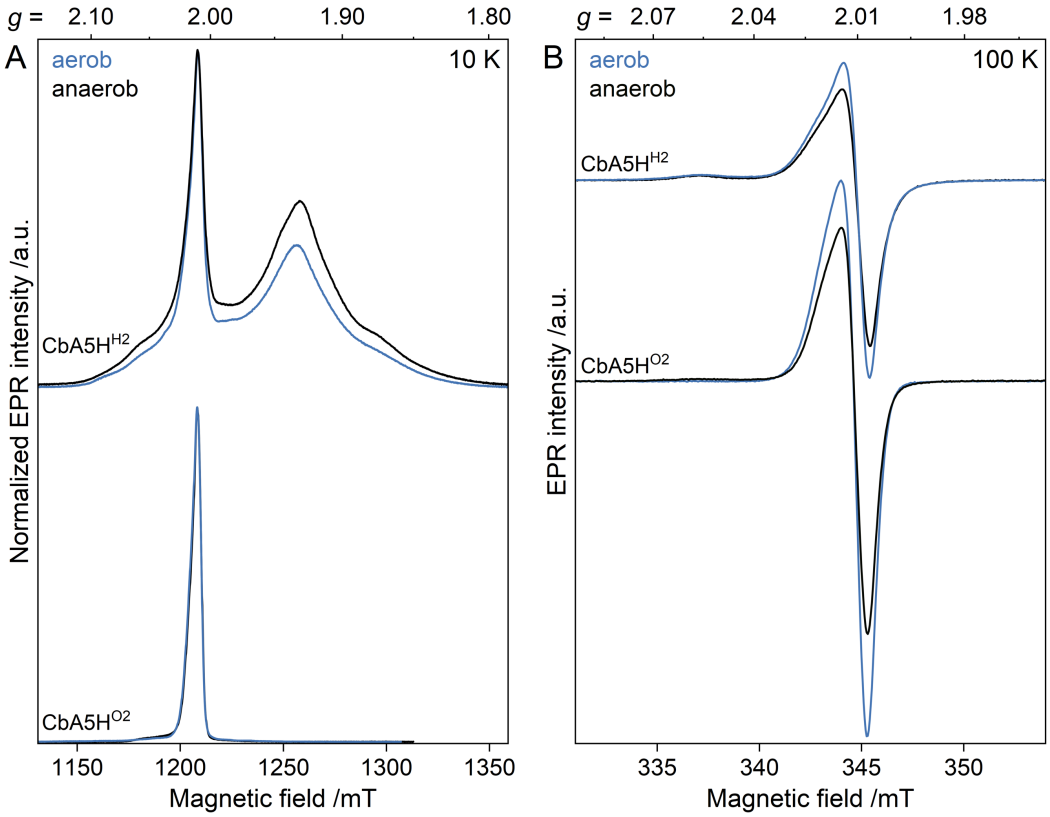

Figure S11. Comparison of EPR spectra of H_2- and O_2-treated CbA5H purified aerobically (blue) and NaDT-free, anaerobically (black). (**A**) Pulsed EPR spectra (34 GHz, T = 10 K) were normalized to their maximum signal intensities to compare the line shapes better. (**B**) Cw EPR spectra (9.7 GHz, T = 100K). At 100 K, spectra of CbA5H^{H2} show a minor contribution from H_{ox}-CO ($g \approx 2.06$). The signal intensities of $R^{\bullet ox}$ obtained via spectral simulations in aerobically purified samples is approximately 22 % higher compared to the anaerobically purified samples. X-band experimental conditions: 10–32 mW power, 1.28–5.12 ms time constant; 60–81 ms conversion time; 45–70 s sweep time, 1–3 scans.

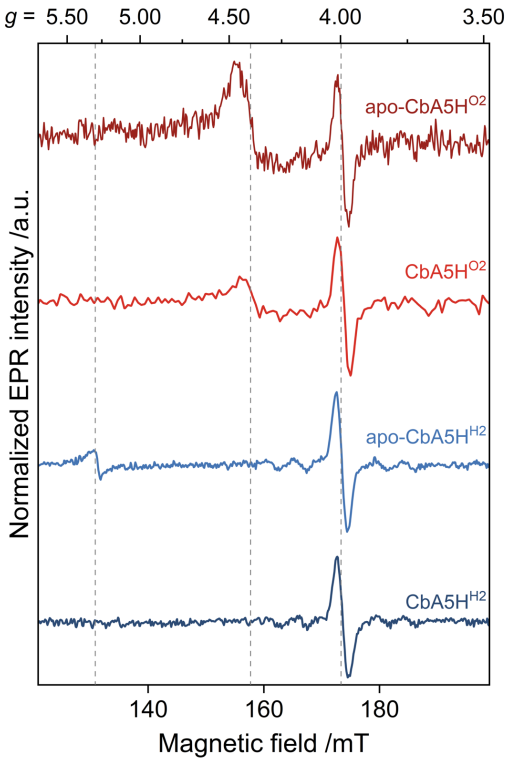

Figure S12. Comparison of cw EPR spectra (9.7 GHz, T = 15–20 K) of apo-CbA5H (730 µM) and holo-CbA5H (970 µM) treated with H_2 and O_2. The grey lines indicate g = 5.3 (left), g = 4.3 (middle, adventitiously bound Fe^{3+} (S = 5/2) [34]) and g = 4 (right, resonator impurity). All spectra were normalized to the resonator impurity signal. The spectrum of $CbA5H^{H2}$ exhibits the resonator impurity only, while apo-$CbA5H^{H2}$ is the only spectrum having a signal at g = 5.3. This indicates the presence of a half-integer high-spin species, as discussed in Ref. [34] and observed in another [FeFe]-hydrogenase under illumination. [13] Spectra of the oxidized samples show varying contributions from adventitiously bound Fe^{3+}. Apo-$CbA5H^{O2}$ has a significantly higher signal intensity at g = 4.3 than holo-$CbA5H^{O2}$. The decreased signal intensity of holo-$CbA5H^{O2}$ at g = 4.3 is noteworthy regarding the $R^{\bullet ox}$ signal, which exhibits one order of magnitude higher signal intensity than the $[3Fe4S]^+$ clusters in apo-$CbA5H^{O2}$ (see Figure S5). Thus, it can be concluded that $R^{\bullet ox}$ is unrelated to the signal intensity at g = 4.3 arising due to degraded FeS clusters. Experimental conditions for (i) H_2-reduced samples: 15 K; 0.47 mW power; 100 ms conversion time and 205 s sweep time and (ii) for O_2-oxidized samples: 15–20 K; 0.047 mW power; 80 ms conversion time and 164 s sweep time.

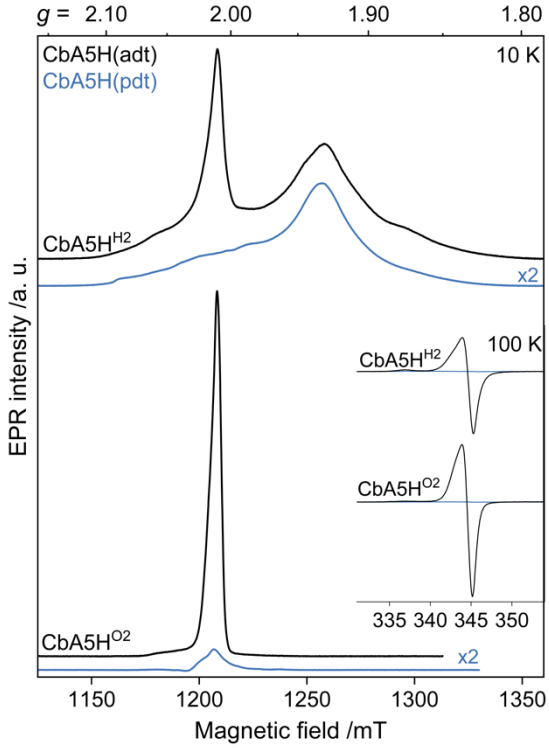

Figure S13. EPR spectra of CbA5H^{H2} and CbA5H^{O2} maturated with adt (490 µM, CbA5H(adt), NaDT-free, black traces) and pdt (500µM, CbA5H(pdt), blue traces). For pulsed EPR spectra (34 GHz, T = 10 K), the intensities of CbA5H(pdt) were multiplied by two for a better comparison of the line shapes. The inset shows the cw EPR spectra (9.7 GHz, T = 100 K) of the same samples. At 10 K, CbA5H(pdt)^{H2} yields H_{ox} as the only paramagnetic H-cluster state and shows contributions from accessory FeS clusters at $g \approx 1.93$. CbA5H(pdt)^{O2} reveals a signal reminiscent of O_2-damaged FeS clusters at lower temperatures. Strikingly, no signal is observed at elevated temperatures in CbA5H(pdt) samples, proving the absence of $R^{\bullet ox}$. X-band experimental conditions: 10 mW power; 1.28 ms time constant; 81 ms conversion time; 77 s sweep time, 3–10 scans.

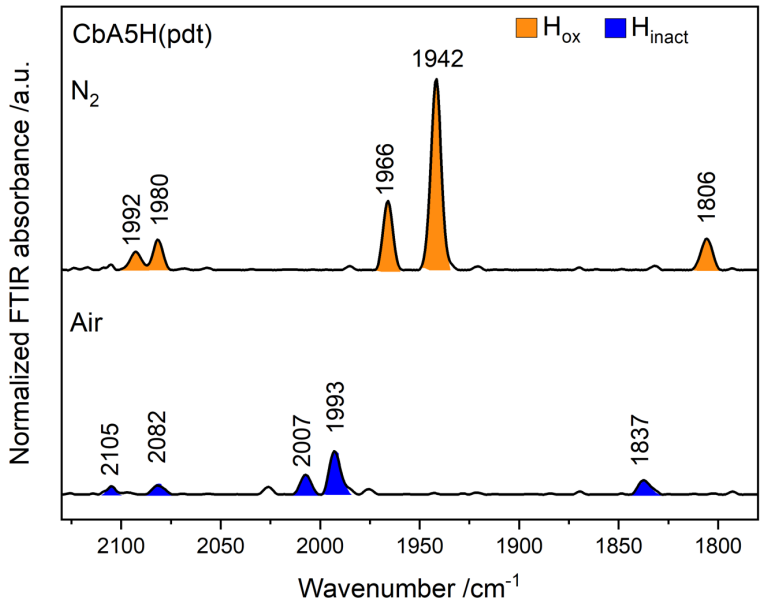

Figure S14. IR-vibrational spectra of CbA5H(pdt) monitored *via* ATR-FTIR-spectroscopy. The upper part of the figure shows CbA5H(pdt) (500 µM, 0.1 M Tris-HCl buffer, pH 8) under a constant stream of N_2 populating the H_{ox} state. The lower part depicts the IR vibrations after purging the same protein film with air (~5 min), showing the presence of H_{inact}.

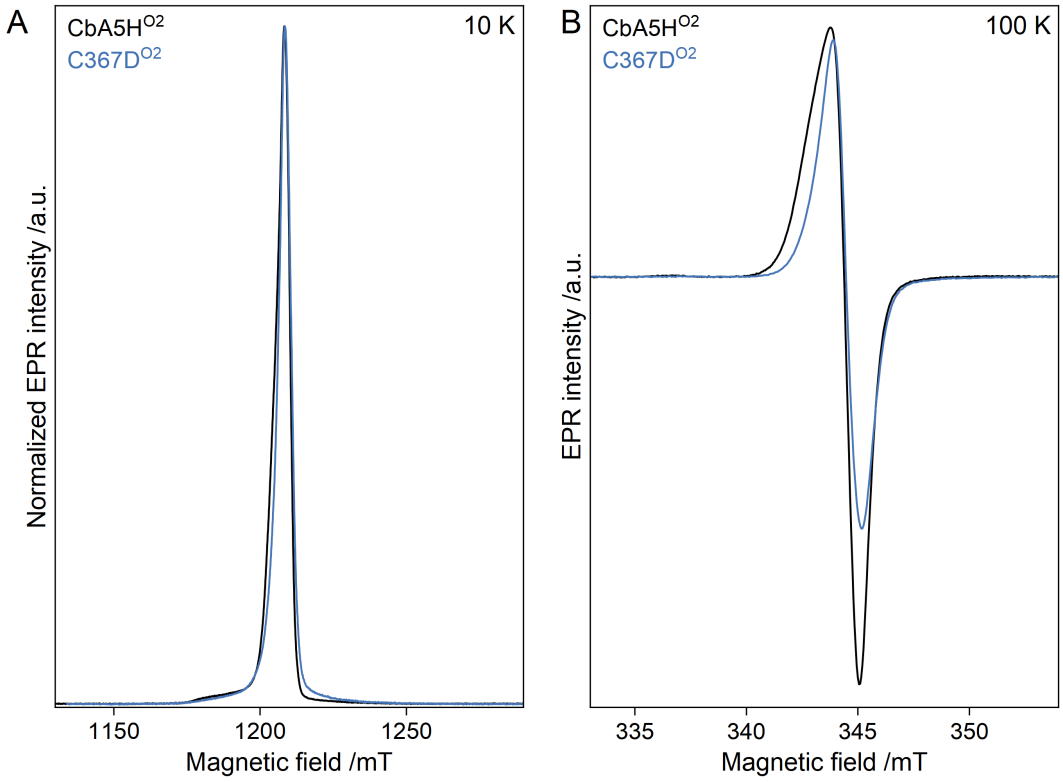

Figure S15. Comparison of EPR spectra of O_2-treated samples of CbA5H (CbA5H^{O2}, NaDT-free, black traces) and its variant C367D (C367D^{O2}, blue traces). (**A**) Pulsed EPR spectra (34 GHz, T = 10 K) were normalized to their maximum signal intensities to compare the line shapes better. (**B**) Cw EPR spectra (9.7 GHz, T = 100K). The C367D variant has a narrower line shape with smaller *g*-values (g = 2.015(3), 2.012(3), 2.007(2)). Additionally, its spin concentration decreased by approximately 35 % compared to wild-type CbA5H^{O2}. X-band experimental conditions for C367D: 32 mW power, 1.28 ms time constant; 82 ms conversion time; 62 s sweep time, 2 scans; for CbA5H^{O2}, see Figure S9.

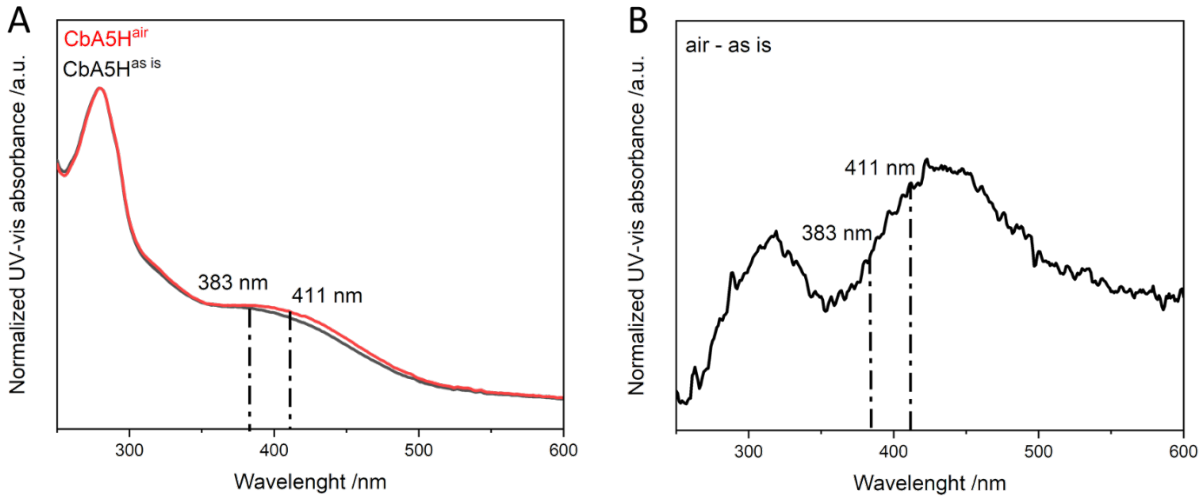

Figure S16. UV-vis and UV-vis difference spectra of as-isolated (black) and air-treated (red) CbA5H. (**A**) Normalized UV-vis spectra (280 nm) of as-isolated protein ($CbA5H^{as\ is}$) and air-treated (10 min) protein solution ($CbA5H^{air}$). The peak at 280 nm represents the absorbance of aromatic amino acids in the protein backbone. Absorbance plateau around 400 nm indicates the presence of FeS clusters. (**B**) UV-vis difference spectra of $CbA5H^{air}$ – $CbA5H^{as\ is}$. Dashed vertical lines indicate expected peak positions for tyrosyl (411 nm) and DOPA (383 nm) radicals which are absent in this spectrum. No decay was observed at 420 nm due to loss of sulfur to iron charge transfer bands. This result shows that the FeS clusters in $CbA5H^{air}$ remain stable upon oxidative treatment and thus, supports the conclusions derived in S8 and S12.

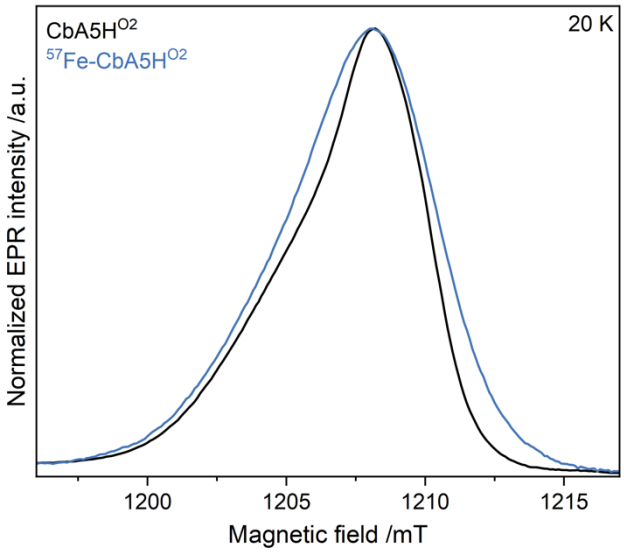

Figure S17. Comparison of pulsed EPR spectra (34 GHz, T = 20 K) of O_2-treated samples of CbA5H (CbA5H^{O2}, NaDT-free, black trace) and ^{57}Fe-labeled CbA5H (^{57}Fe-CbA5H^{O2}, blue traces). The spectra were normalized to their maximum signal intensities to better compare the line shapes. The hyperfine interactions with ^{57}Fe nuclei lead to a broadening of the line shape.

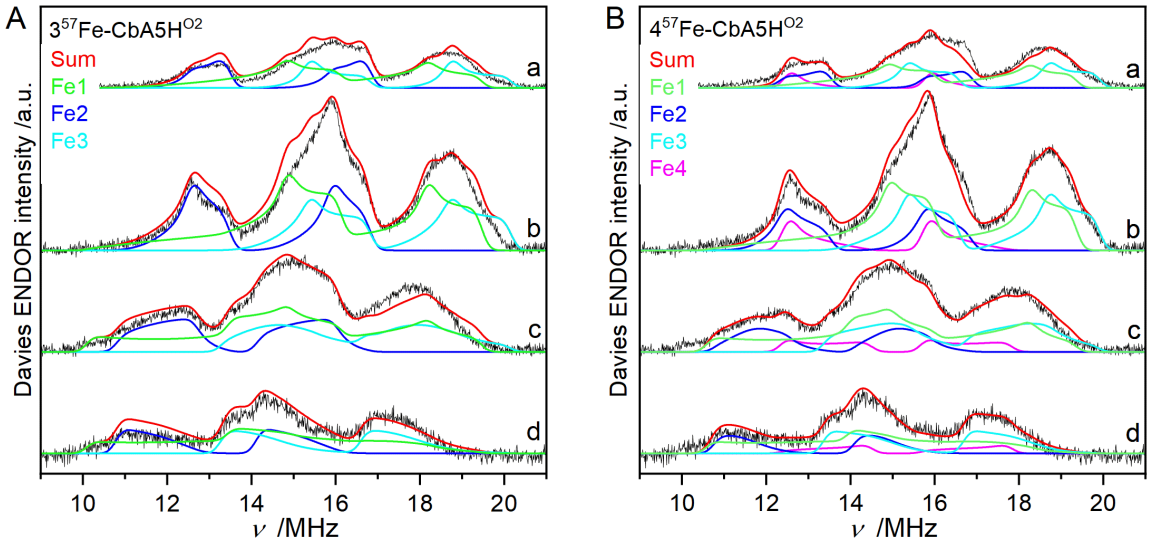

Figure S18. Davies ^{57}Fe ENDOR spectra (Q-band, T = 20 K) of ^{57}Fe-labeled CbA5H^{O2} at different field positions and respective spectral simulations. a: g = 2.008 **b:** g = 2.012 **c:** g = 2.018 **d:** g = 2.022. The simulations were performed with a global fitting function using *salt* in Easy spin and employing (**A**) 3 ^{57}Fe nuclei or (**B**) 4 ^{57}Fe nuclei. The obtained simulation parameters in comparison to literature parameters are displayed in Table S4.

Table S4. Simulation parameters for ^{57}Fe nuclei found in R$^{\bullet ox}$ from ^{57}Fe-labeled CbA5H and in H$_{ox}$-CO from different organisms.

Species	Nuclei	A_x	A_y	A_z	$\lvert A_{iso}\rvert$	φ (deg)	θ (deg)	ψ (deg)	Reference
3Fe-R$^{\bullet ox}$	Fe1	28.5	24.9	30.3	27.9	101	10	6	this work
	Fe2	29.8	34.2	37.0	33.7	89	103	81	
	Fe3	23.5	33.1	35.6	30.7	105	80	59	
4Fe-R$^{\bullet ox}$	Fe1	28.0	32.4	28.5	29.6	62	199	2	this work
	Fe2	28.3	24.8	30.4	27.8	88	0	0	
	Fe3	30.0	34.1	36.5	33.6	89	62	74	
	Fe4	24.5	33.2	35.4	31.0	82	98	60	
H$_{ox}$-CO[a]	Fe1	29.9	35.1	25.1	30.0	8	0	0	[35]
	Fe2	31.2	37.3	31.2	33.2	0	0	0	
	Fe3	28.6	24.7	30.8	28.0	110	0	0	
	Fe4	23.5	29.6	29.8	27.6	20	0	0	
H$_{ox}$-CO[b]	Fe1	-35.4	-35.0	-30.4	33.6	90	185	-	[36]
	Fe2	-34.5	-38.4	-30.7	34.5	90	5	-	
	Fe3	+27.8	+21.8	+30.3	26.7	5	110	-	
	Fe4	+26.7	+23.8	+30.2	27.0	76	-93	-	

[a] from *C. reinhardtii*

[b] from *D. desulfuricans*

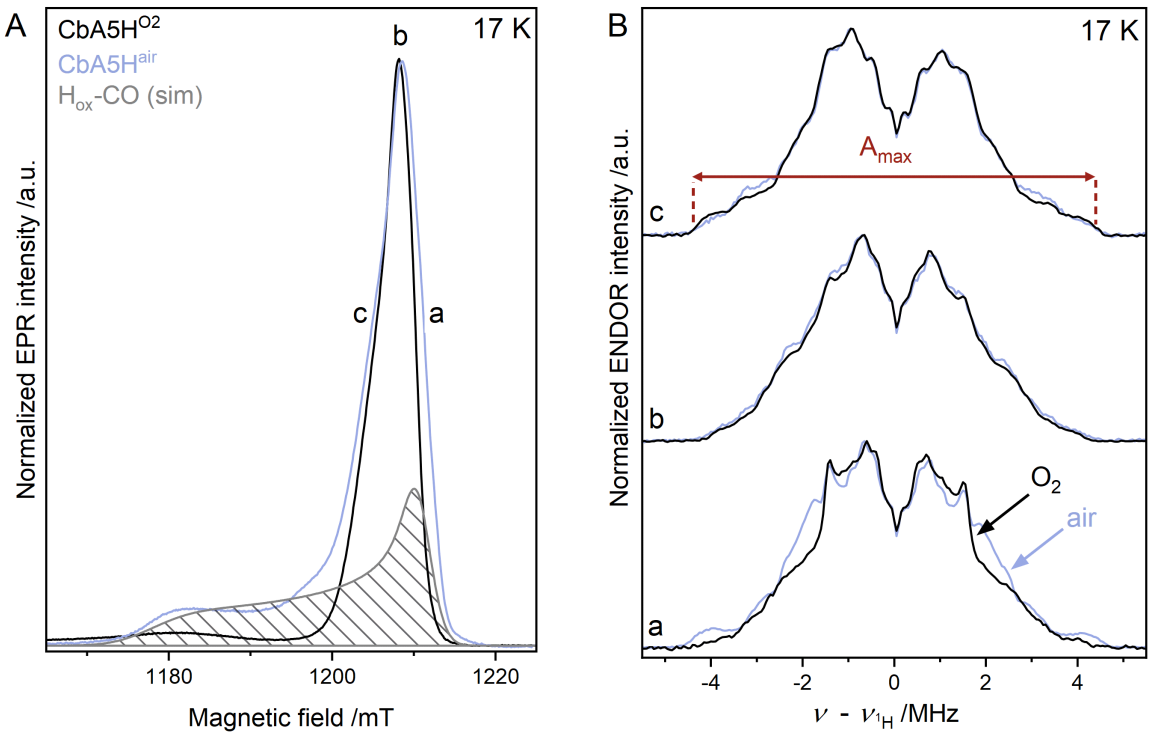

Figure S19. Comparison of EPR and ENDOR spectra of O_2-treated CbA5H (CbA5H^{O2}, NaDT-free, thawed once, black traces) and air-treated CbA5H (CbA5H^{air}, thawed once, blue traces). (**A**) Pulsed EPR spectra (34 GHz, T = 17 K) were normalized to their maximum signal intensities to compare the line shapes better. The simulation of CbA5H^{air} comprises contributions from R$^{\bullet ox}$ (56 % relative weight, not shown) and H_{ox}-CO (44 % relative weight, grey pattern). The field positions **a** (g = 2.008), **b** (g = 2.012) and **c** (g = 2.018) at which the ENDOR spectra were recorded are indicated. (**B**) Proton Davies ENDOR (Q-band, T = 17 K) of CbA5H^{O2} and CbA5H^{air} recorded at the three field positions given in (A). The maximum hyperfine coupling value A_{max} of CbA5H^{O2} is approximately 9 MHz (red arrow). Comparing ^{1}H ENDOR data of CbA5H^{O2} and CbA5H^{air} recorded at positions **c** and **b** revealed only insignificant differences. Yet, ^{1}H ENDOR data of CbA5H^{air} recorded at position **a** shows additional features compared to those of CbA5H^{O2}. These additional low-intensity signals arise from the underlying H_{ox}-CO present in the CbA5H^{air} sample. These data demonstrate unambiguously that the hyperfine couplings detected for CbA5H^{O2} belong solely to R$^{\bullet ox}$. Note that the differences between CbA5H^{O2} and CbA5H^{air} are only prominent at position **a** because the ratio of H_{ox}-CO to R$^{\bullet ox}$ contributing to the ENDOR spectrum at this orientation is the highest, as can be seen in (A). The identical multiplication factors used to normalize the EPR, and ^{1}H ENDOR spectra of ^{57}Fe-CbA5H^{O2} to those of CbA5H^{O2} strongly support the conclusion that the hyperfine couplings observed for CbA5H^{O2} are due to R$^{\bullet ox}$ (see S20).

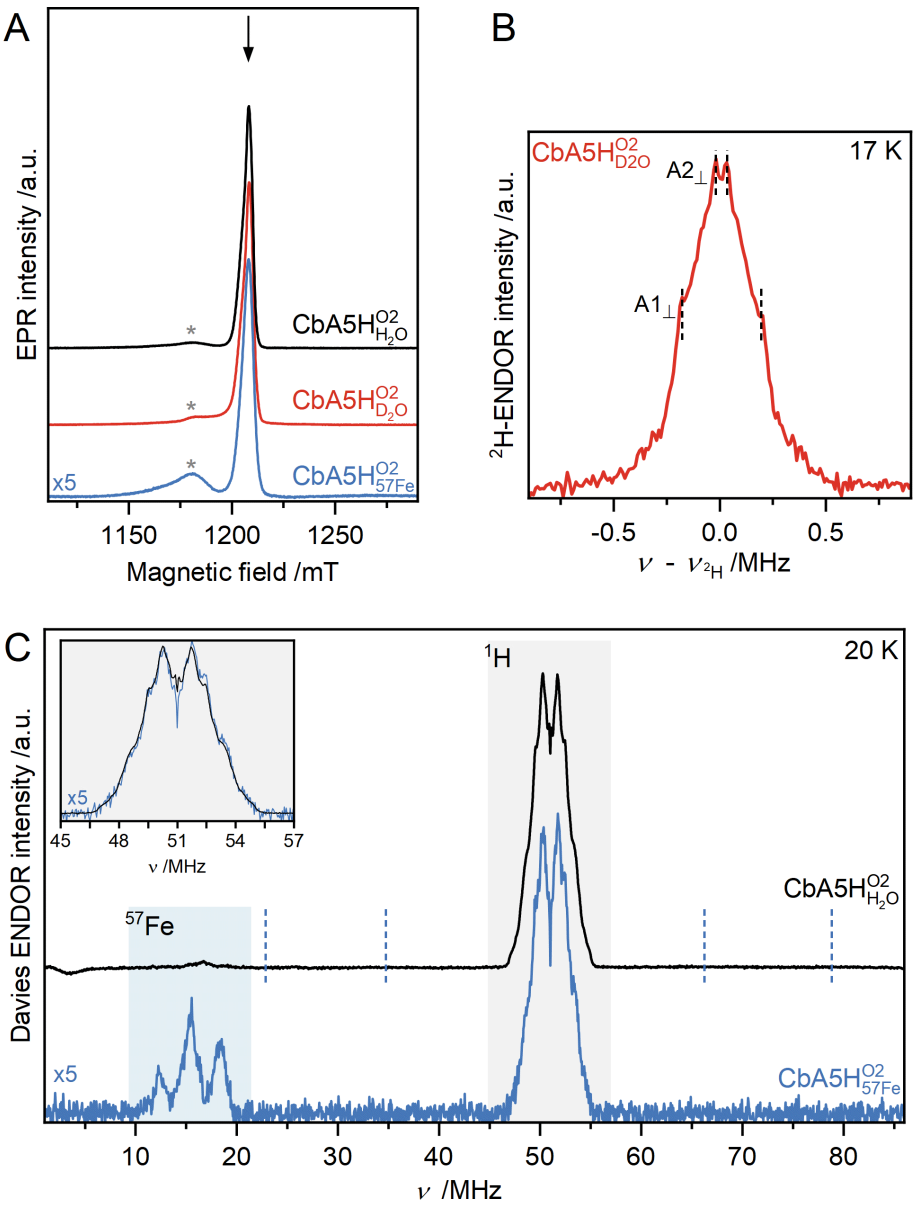

Figure S20. EPR and ENDOR spectra of CbA5H^{O2} in protonated (CbA5H$_{H2O}$) and deuterated (CbA5H$_{D2O}$) buffer and maturated with ^{57}Fe (^{57}Fe-CbA5H) (T = 17/20 K, 34 GHz). The sample of CbA5H$_{H2O}$ had undergone cryo-annealing before the ENDOR experiments (see Figure S5 D). Both CbA5H$_{H2O}$ and CbA5H$_{D2O}$ were subsequently thawed and transferred into 1.6 mm tubes for the ENDOR measurements shown here and in Figure S19. The spectral intensity of ^{57}Fe-CbA5H was multiplied by five in each spectrum. (**A**) ESE-detected EPR spectra (34 GHz, T = 17/20K). The asterisks mark residual H$_{ox}$-CO and/or resonator impurity signals. The arrow indicates the field position at which the ENDOR spectra were recorded. (**B**) Mims ^{2}H ENDOR spectrum (Q-band, T = 17 K) of CbA5H$_{D2O}$. At least two different couplings are observable as marked by black vertical dashed lines showing the perpendicular components of the hyperfine couplings (A$_\perp$). (**C**) Comparison of Davies ENDOR spectra of CbA5H^{O2} (black trace) and ^{57}Fe-CbA5H^{O2} (blue trace) recorded with a 40 µs RF pulse ranging from 1 to 86 MHz. The inset shows the comparison of hyperfine couplings arising from protons. The almost identical line shapes detected for CbA5H^{O2,} and ^{57}Fe-CbA5H^{O2} show that ^{57}Fe enrichment does not disturb the H-bonding environment and structure of R$^{\bullet ox}$. CbA5H^{O2} does not exhibit strong ^{1}H hyperfine couplings (grey area and inset), which could be associated with tyrosyl and natural DOPA radicals and would be observed at positions marked with vertical dashed blue lines. [37,38] Additionally, the typical ^{14}N hyperfine coupling values observed with natural tryptophanyl radicals are approximately 28 MHz. [39] This coupling would give rise to spectral patterns at $\nu \approx 15$ MHz (blue shaded area). [40] Neither strong ^{1}H nor ^{14}N hyperfine couplings are observed in this spectrum, excluding a typical tyrosyl, DOPA, or tryptophanyl radical as the origin of R$^{\bullet ox}$.

Supporting Discussion on the identity of $R^{\bullet ox}$

Amino-acid-based radicals, e.g., derived from tyrosine, tryptophan, cysteine, and glycine serve as redox centers, generating important metabolites in radical enzymes, such as galactose oxidase ribonucleotide reductase, cytochrome *c* peroxidase, and pyruvate formate-lyase. [41] As the *g*-values of $R^{\bullet ox}$ and its temperature dependence are reminiscent of organic radicals; we investigated whether a redox-active amino acid residue can be the source of the $R^{\bullet ox}$ signal. However, the characteristics of our EPR and UV-vis data conflict with those of typical amino acid radicals. First, the *g*-shifts ($\Delta g_i = g_i - g_e$) of $R^{\bullet ox}$ are too large for a free tyrosyl/modified tyrosyl (natural DOPA or DOPA radical anion), glycyl or tryptophanyl radical but too small to be associated with a thiyl radical. [24,42] Second, distinct peaks related to either tyrosyl or natural DOPA radicals are not observed in the UV-vis spectra of $R^{\bullet ox}$ (Figure S16). Third, ^1H Davies ENDOR spectra of $R^{\bullet ox}$ in H_2O and D_2O revealed numerous non-exchangeable proton hyperfine couplings smaller than 10 MHz (Figure S19, the largest hyperfine coupling constant value that is approximately 9 MHz is read between vertical dashed lines). The absence of strong proton and nitrogen hyperfine couplings contrasts the literature data of typical tyrosyl, glycyl, thiyl, and tryptophanyl radicals (Figure S20). [24,43]

Next, we considered sulfur-based radicals because the increased $R^{\bullet ox}$ *g*-anisotropy ($\Delta g = g_3 - g_1 = 13 \cdot 10^{-3}$), usually originating from a large spin-orbit coupling, is indicative of such radicals. [44,45] The *g*-values of $R^{\bullet ox}$ differ from those of disulfide radical anions but agree with *g*-values of sulfinyl or sulfonyl radicals. [44] Similar to $R^{\bullet ox}$, the latter have been observed as reversible intermediates. [46–50] However, the associated proton hyperfine coupling constants are greater than 10 MHz and dominate the line shape at lower frequencies, which is not observed for $R^{\bullet ox}$. Therefore, it is unlikely that $R^{\bullet ox}$ is a typical sulfur-based radical.

Apart from the free amino acid radicals discussed above, several unusual ones have been reported. [41] These include modified amino acids and amino acid radicals having anomalous spectroscopic properties due to their interaction with a close-by metallocofactor. One example is the tryptophan cation radical found in cytochrome *c* peroxidase, namely $Trp191^{\bullet +}$, having a weak exchange coupling with the oxyferryl-heme. [51], [52] Surprisingly, *g*-values of $R^{\bullet ox}$ and $Trp191^{\bullet +}$ are highly similar, and strong ^{14}N hyperfine couplings are absent in both. Yet, the largest proton hyperfine coupling component detected for $Trp191^{\bullet +}$ is higher than that of $R^{\bullet ox}$ (ca. 20 MHz *vs.* 9 MHz).

Last, we note that the reversibility of $R^{\bullet ox}$, and its ENDOR spectrum, showing various proton hyperfine couplings, exclude the possibility of a peroxyl radical. In addition, a semiquinone radical is highly unlikely as the *g*-shifts observed for this radical are remarkably small compared to those of $R^{\bullet ox}$.

References

[1] S. Stoll and A. Schweiger, J. Magn. Reson. **178**, 42 (2006).

[2] M. K. Akhtar and P. R. Jones, Appl. Microbiol. Biotechnol. **78**, 853 (2008).

[3] J. M. Kuchenreuther, C. S. Grady-Smith, A. S. Bingham, S. J. George, S. P. Cramer, and J. R. Swartz, PLoS One **5**, 4 (2010).

[4] M. Bradford, Anal. Biochem. **72**, 248 (1976).

[5] U. K. Laemmli, Nature **227**, 680 (1970).

[6] P. S. Corrigan, J. L. Tirsch, and A. Silakov, J. Am. Chem. Soc. **142**, 12409 (2020).

[7] H. Li and T. B. Rauchfuss, J. Am. Chem. Soc. **124**, 726 (2002).

[8] J. Esselborn et al., Nat. Chem. Biol. **9**, 607 (2013).

[9] D. W. Mulder, Y. Guo, M. W. Ratzloff, and P. W. King, J. Am. Chem. Soc. **139**, 83 (2017).

[10] G. Rao and R. D. Britt, Inorg. Chem. **57**, 10935 (2018).

[11] A. Adamska, A. Silakov, C. Lambertz, O. Rüdiger, T. Happe, E. Reijerse, and W. Lubitz, Angew. Chemie - Int. Ed. **51**, 11458 (2012).

[12] H. Land, M. Senger, G. Berggren, and S. T. Stripp, ACS Catal. **10**, 7069 (2020).

[13] S. P. J. Albracht, W. Roseboom, and E. C. Hatchikian, J. Biol. Inorg. Chem. **11**, 88 (2006).

[14] H. J. Grande, W. R. Dunham, B. Averill, C. Dijk, and R. H. Sands, Eur. J. Biochem. **136**, 201 (1983).

[15] W. R. Hagen, A. van Berkel-Arts, K. M. Krüse-Wolters, W. R. Dunham, and C. Veeger, FEBS Lett. **201**, 158 (1986).

[16] D. S. Patil, S. H. He, J. J. G. Mouras, N. Ravi, D. V. DerVartanian, H. D. Peck, J. LeGall, and B. H. Huynh, J. Inorg. Biochem. **36**, 251 (1989).

[17] B. Bennett, B. J. Lemon, and J. W. Peters, Biochemistry **39**, 7455 (2000).

[18] G. Caserta, A. Adamska-Venkatesh, L. Pecqueur, M. Atta, V. Artero, S. Roy, E. Reijerse, W. Lubitz, and M. Fontecave, Biochim. Biophys. Acta - Bioenerg. **1857**, 1734 (2016).

[19] R. Cammack, *Iron—Sulfur Clusters in Enzymes: Themes and Variations*, in *Advances in Inorganic Chemistry*, Vol. 38 (1992), pp. 281–322.

[20] H. Rupp, K. K. Rao, D. O. Hall, and R. Cammack, Biochim. Biophys. Acta - Protein Struct. **537**, 255 (1978).

[21] M. Atta, M. E. Lafferty, M. K. Johnson, J. Gaillard, and J. Meyer, Biochemistry **37**, 15974 (1998).

[22] T. Liu, B. Li, M. L. Singleton, M. B. Hall, and M. Y. Darensbourg, J. Am. Chem. Soc. **131**, 8296 (2009).

[23] K. D. Swanson et al., J. Am. Chem. Soc. **137**, 1809 (2015).

[24] G. Jeschke, Biochim. Biophys. Acta - Bioenerg. **1707**, 91 (2005).

[25] N. Chongdar, K. Pawlak, O. Rüdiger, E. J. Reijerse, P. Rodríguez-Maciá, W. Lubitz, J. A. Birrell, and H. Ogata, J. Biol. Inorg. Chem. (2019).

[26] M. L. Antonkine, M. S. Koay, B. Epel, C. Breitenstein, O. Gopta, W. Gärtner, E. Bill, and W. Lubitz, Biochim. Biophys. Acta - Bioenerg. **1787**, 995 (2009).

[27] P. Rodríguez-Maciá, K. Pawlak, O. Rüdiger, E. J. Reijerse, W. Lubitz, and J. A. Birrell, J. Am. Chem. Soc. **139**, 15122 (2017).

[28] M. Winkler et al., Nat. Commun. **12**, 756 (2021).

[29] J. A. Imlay, Mol. Microbiol. **59**, 1073 (2006).

[30] J. Telser, H.-I. Lee, and B. M. Hoffman, J. Biol. Inorg. Chem. **5**, 369 (2000).

[31] S. Agarwalla, R. M. Stroud, and B. J. Gaffney, J. Biol. Chem. **279**, 34123 (2004).

[32] M. Saggu, I. Zebger, M. Ludwig, O. Lenz, B. Friedrich, P. Hildebrandt, and F. Lendzian, J. Biol. Chem. **284**, 16264 (2009).

[33] M. T. Pellicer Martinez, J. C. Crack, M. Y. Y. Stewart, J. M. Bradley, D. A. Svistunenko, A. W. B. Johnston, M. R. Cheesman, J. D. Todd, and N. E. Le Brun, Elife **8**, 1 (2019).

[34] W. R. Hagen, *EPR Spectroscopy of Iron—Sulfur Proteins*, in *Advances in Inorganic Chemistry*, Vol. 38 (1992), pp. 165–222.

[35] R. Gilbert-Wilson, J. F. Siebel, A. Adamska-Venkatesh, C. C. Pham, E. Reijerse, H. Wang, S. P. Cramer, W. Lubitz, and T. B. Rauchfuss, J. Am. Chem. Soc. **137**, 8998 (2015).

[36] A. Silakov, E. J. Reijerse, S. P. J. Albracht, E. C. Hatchikian, and W. Lubitz, J. Am. Chem. Soc. **129**, 11447 (2007).

[37] V. Srinivas et al., Nature **563**, 416 (2018).

[38] S. L. Meichsner, Y. Kutin, and M. Kasanmascheff, Angew. Chemie - Int. Ed. **60**, 19155 (2021).

[39] R. Pogni, M. C. Baratto, C. Teutloff, S. Giansanti, F. J. Ruiz-Dueñas, T. Choinowski, K. Piontek, A. T. Martínez, F. Lendzian, and R. Basosi, J. Biol. Chem. **281**, 9517 (2006).

[40] S. M. Musser, Y.-C. Fann, R. J. Gurbiel, B. M. Hoffman, and S. I. Chan, J. Biol. Chem. **272**, 203 (1997).

[41] J. A. Stubbe and W. A. Van Der Donk, Chem. Rev. **98**, 705 (1998).

[42] S. Stoll, *High-Field EPR of Bioorganic Radicals*, in *Electron Paramagnetic Resonance*, Vol. 22 (Royal Society of Chemistry, 2011), pp. 107–154.

[43] M. van Gastel, W. Lubitz, G. Lassmann, and F. Neese, J. Am. Chem. Soc. **126**, 2237 (2004).

[44] N. Babaei Bidmeshki, Y. T. Azar, F. Ziaie, and M. Janbazi, Phys. Chem. Chem. Phys. **23**, 6815 (2021).

[45] S. G. Swarts, D. Becker, S. DeBolt, and M. D. Sevilla, J. Phys. Chem. **93**, 155 (1989).

[46] A. Adrait, M. Öhrström, A.-L. Barra, L. Thelander, and A. Gräslund, Biochemistry **41**, 6510 (2002).

[47] S. G. Reddy, K. K. Wong, C. V. Parast, J. Peisach, R. S. Magliozzo, and J. W. Kozarich, Biochemistry **37**, 558 (1998).

[48] G. Lassmann, M. Kolberg, G. Bleifuss, A. Gräslund, B.-M. Sjöberg, and W. Lubitz, Phys. Chem. Chem. Phys. **5**, 2442 (2003).

[49] M. D. Sevilla, D. Becker, and M. Yan, Int. J. Radiat. Biol. **57**, 65 (1990).

[50] M. Kolberg, G. Bleifuss, B.-M. Sjöberg, A. Gräslund, W. Lubitz, F. Lendzian, and G. Lassmann, Arch. Biochem. Biophys. **397**, 57 (2002).

[51] M. Sivaraja, D. B. Goodin, M. Smith, and B. M. Hoffman, Science **245**, 738 (1989).

[52] A. L. P. Houseman, P. E. Doan, D. B. Goodwin, and B. M. Hoffman, Biochemistry **32**, 4430 (1993).